Stokes' second problem with wall suction or blowing for UCM fluids

D.O.A. Cruz [a], F.T. Pinho [b,c,*]

[a] *Departamento de Engenharia Mecânica, Universidade Federal do Pará- UFPa, Campus Universitário do Guamá, 66075-900 Belém, Pará, Brazil*
[b] *Centro de Estudos de Fenómenos de Transporte, FEUP, Rua Dr. Roberto Frias s/n, 4200-465 Porto, Portugal*
[c] *Universidade do Minho, Largo do Paço, 4704-553 Braga, Portugal*

ARTICLE INFO

ABSTRACT

An analytical solution is derived for the time-dependent flow of an infinite pool of fluid described by the viscoelastic upper convected Maxwell (UCM) model driven by an oscillating porous plate in the presence of cross flow. Whereas for a Newtonian fluid there is a solution regardless of the amount of suction or blowing, for viscoelastic fluids the solution breaks down under certain conditions. When the suction velocity exceeds the elastic shear wave speed there is no solution. For sub-critical blowing through the plate the stream-wise velocity profiles are periodic, but when the blowing speed exceeds the elastic shear wave speed non-periodic chaotic-like waves appear under certain conditions, which are characterized. The flow characteristics are properly scaled by the reciprocal square root of the Reynolds number with and without cross flow. Generally speaking, the flow properties are controlled by the cross flow and by the fluid elasticity at low and high Deborah numbers, respectively.

© 2008 Elsevier B.V. All rights reserved.

1. Introduction

The time-dependent flow of viscoelastic fluids caused by the oscillation of a flat plate is of considerable interest both industrially as well as a test case to assess the performance of numerical methods for the computation of transient flows. Indeed, as demonstrated by Oliveira [1], the performance of time discretization numerical methods needs to be assessed not only against time-dependent solutions, such as the start-up of flows, but also against unsteady flows of unlimited duration in order to better assess the accuracy of the methods and the accumulation of errors over time. Periodic flows are useful in this respect.

A fundamental viscoelastic model of differential type is the upper convected Maxwell fluid (UCM), which models the polymer contribution of some types of Boger fluids [2] and polymer melts of constant viscosity. The solution of Stokes' second problem for this fluid has been addressed recently by Hayat et al. [3] and Aksel et al. [4], using Fourier series. These works also include other analytical solutions for the same fluids, namely: the Stokes problem for bounded flows, periodic Poiseuille flows due to oscillating pressure gradient as well as the start-up Poiseuille flow. Actually, the start-up Poiseuille flow for the Oldroyd-B fluid was derived by

Waters and King [5] for a pipe and by Mochimaru [6] for the flow between parallel plates. Regarding the plate bounded by an infinite body of fluid, Tanner [7] worked on Stokes' first problem for Oldroyd-B fluids and showed that for UCM fluids the shear wave propagated away from the plate at a constant speed $c = \sqrt{\eta/\rho\lambda}$, where η, ρ and λ represent the viscosity coefficient, the density and relaxation time of the fluid, respectively. The solutions of Hayat et al. [3] and Aksel et al. [4] for Stokes' second problem include also the start-up from rest of the periodic oscillating flow, an issue which seems to have been pioneered by Erdogan [8] for Newtonian fluids.

Given the non-linear nature of the viscoelastic constitutive equation for the Oldroyd-B fluid and the non-linear nature of the additional term of the momentum equation, the solution of Stokes' second problem with suction/blowing through a porous wall is not simply the linear combination of the two simpler solutions, although the non-linearity in the momentum equation is eliminated by consideration of a constant suction/blowing velocity. As far as we are aware of, the solution of this more complex flow is not available in the literature for viscoelastic fluids and this paper presents the theoretical solution for the flow resulting from the combination of a sinusoidal tangential oscillation of a wall with constant flow suction/blowing normal to the wall.

The paper is organized as follows. Section 2 presents the governing equations and the corresponding boundary and initial conditions. The derivation of the analytical solution is explained in Section 3 and the paper discusses some interesting results in Section 4, prior to the closure of this paper.

* Corresponding author at: Centro de Estudos de Fenómenos de Transporte, DEMEGI, FEUP, Rua Dr. Roberto Frias s/n, 4200-465 Porto, Portugal.
Tel.: +351 225081597; fax: +351 225082153/1440.
E-mail addresses: doac@ufpa.br (D.O.A. Cruz), fpinho@fe.up.pt (F.T. Pinho).

2. Governing equations and boundary conditions

The flow under consideration is created by a plate perpendicular to the y-axis, oscillating in the x-direction and the fluid is in the region $y \geq 0$. The plate is porous and the suction/blowing is characterized by a constant time-independent velocity v_w ($v_w > 0$ for blowing; $v_w < 0$ for suction). The equations will be presented in normalized form for which the following scales are used: the characteristic velocity is the amplitude of the velocity oscillation of the plate (U_0); the characteristic length is U_0/ω, where ω is the frequency of oscillation of the plate, time is normalized as ωt and the stresses are normalized by $\eta_p \omega$, where η_p stands for the polymer viscosity coefficient. The normalization of the equations gives rise to some well known non-dimensional numbers, such as the Reynolds (Re) and Deborah (De) numbers, which are defined as $Re = \rho U_0^2 / \omega \eta_p$ and $De = \lambda \omega$, respectively, with λ being the relaxation time of the polymer. Other non-dimensional quantities help understand the flow physics and are introduced next.

The propagation of shear waves in elastic fluids at rest takes place at a well defined velocity $c = \sqrt{\eta_p / \rho \lambda}$, therefore leading to the definition of an elastic Mach number (M), the ratio of the characteristic velocity to the wave speed. It is easy to demonstrate that this leads to $M = \sqrt{Re \times De}$. Another non-dimensional parameter that helps understand the dynamics of viscoelastic flows is the elasticity number (E), which has several interpretations (see chapter 7 in Joseph [9]). E is defined as the ratio between the Deborah and Reynolds numbers ($E = De/Re$) and is usually viewed as the ratio of elastic to viscous forces, but given the choice of scales adopted, here it is more accurate to interpret it as the ratio between elastic to inertial forces. Also, instead of the more classical alternative interpretation as the square of the ratio of two lengths over a relaxation time period, namely the diffusion length and the length traveled by shear waves, here E should be interpreted as the square of the ratio between an elastic length scale and the amplitude length of the oscillation, with the former defined on the basis of the relaxation time and the latter using the period of oscillation. Finally, sometimes it will also be useful to work with an injection Mach number ($M_w \equiv v_w \sqrt{Re \times De}$) instead of the normalized suction/injection velocity v_w, as will become apparent in the presentation of results. The relevance of M_w is clear as it naturally arises from the equations.

The normalised momentum equation for this unsteady flow is

$$\frac{\partial u}{\partial t} + v_w \frac{\partial u}{\partial y} = \frac{1}{Re} \frac{\partial \tau_{xy,p}}{\partial y} \tag{1}$$

with the polymer shear stress ($\tau_{yx} = \tau_{xy}$) given by the UCM differential constitutive equation having a relaxation time λ and a viscosity coefficient η_p, as mentioned above.

For an UCM fluid, the polymer extra stress tensor is written in index notation and in non-dimensional form as in Eq. (2):

$$\tau_{ij,p} + De \left(\frac{\partial \tau_{ij,p}}{\partial t} + u_k \frac{\partial \tau_{ij,p}}{\partial x_k} - \tau_{jk,p} \frac{\partial u_i}{\partial x_k} - \tau_{ik,p} \frac{\partial u_j}{\partial x_k} \right) = \frac{\partial u_i}{\partial x_j} + \frac{\partial u_j}{\partial x_k} \tag{2}$$

Eq. (2) simplifies to the following set, where for convenience the subscript p has been dropped.

$$De \left(\frac{\partial \tau_{xy}}{\partial t} + v_w \frac{\partial \tau_{xy}}{\partial y} - \frac{\partial u}{\partial y} \tau_{yy} \right) + \tau_{xy} = \frac{\partial u}{\partial y} \tag{3-a}$$

$$De \left(\frac{\partial \tau_{yy}}{\partial t} + v_w \frac{\partial \tau_{yy}}{\partial y} \right) + \tau_{yy} = 0 \tag{3-b}$$

$$De \left(\frac{\partial \tau_{xx}}{\partial t} + v_w \frac{\partial \tau_{xx}}{\partial y} - 2 \frac{\partial u}{\partial y} \tau_{xy} \right) + \tau_{xx} = 0 \tag{3-c}$$

This is further simplified by considering that $\tau_{yy} = 0$ (cf. Appendix A). The equations to be solved are subject to the following boundary and initial conditions:

At $y = 0$, $u(0, t) = e^{it}$ (4-a)

At $y = \infty$, $u(\infty, t) = 0$ (4-b)

At $t < 0$, $u(y, t) = 0$ (4-c)

3. Analytical solution

The second assumption made here is that $u = u(\phi)$, $\tau_{xx} = \tau_{xx}(\phi)$ and $\tau_{xy} = \tau_{xy}(\phi)$, where $\phi = At + By$, and Eqs. (1), (2), (3-a) and (3-c) become Eqs. (5-a)–(5-c).

$$(A + v_w B) \frac{du}{d\phi} = \frac{B}{Re} \frac{d\tau_{xy}}{d\phi} \tag{5-a}$$

$$De(A + v_w B) \frac{d\tau_{xy}}{d\phi} + \tau_{xy} = B \frac{du}{d\phi} \tag{5-b}$$

$$De \left[(A + v_w B) \frac{d\tau_{xx}}{d\phi} - 2B \frac{du}{d\phi} \tau_{xy} \right] + \tau_{xx} = 0 \tag{5-c}$$

Using Eq. (5-b) to eliminate $du/d\phi$ in Eq. (5-a) and rearranging provides the following differential equation for τ_{xy}:

$$\left[De(A + v_w B) - \frac{B^2}{Re(A + v_w B)} \right] \frac{d\tau_{xy}}{d\phi} + \tau_{xy} = 0 \tag{6}$$

Defining $1/\alpha = A + v_w B$ and making $1/z = De(A + v_w B) - (B^2/Re(A + v_w B)) = (De/\alpha - \alpha B^2/Re)$, the integration of Eq. (6) provides the shear stress distribution of Eq. (7), where c_1 is to be determined later from a boundary condition.

$$\tau_{xy} = e^{-z\phi + c_1} \tag{7}$$

This shear stress and its derivative are back-substituted into Eq. (5-a), which provide the velocity derivative ($du/d\phi$) and the velocity distribution after integration, as follows:

$$\frac{du}{d\phi} = \frac{B}{Re(A + v_w B)} (-z) e^{-z\phi + c_1} \rightarrow u = \frac{B}{Re(A + v_w B)} e^{-z\phi + c_1} + c_2$$

$$= \frac{B\alpha}{Re} e^{-z\phi + c_1} \tag{8}$$

where $c_2 = 0$ on account of the boundary condition $u(\infty, t) = 0$.

To obtain a differential equation on the normal stress τ_{xx}, $du/d\phi$ from Eq. (8) and τ_{xy} from Eq. (7) are substituted into Eq. (5-c) and rearranged to give

$$\frac{De}{\alpha} \frac{d\tau_{xx}}{d\phi} + \tau_{xx} = -2z \frac{De B^2 \alpha}{Re} e^{-2z\phi + 2c_1} \tag{9}$$

Multiplying by $e^{(\alpha/De)\phi}$ gives

$$\frac{d}{d\phi} \left(e^{(\alpha/De)\phi} \tau_{xx} \right) = -2z \frac{B^2 \alpha^2}{Re} e^{\phi(-2z + \alpha/De) + 2c_1} \tag{10}$$

and integrating provides the following normal stress distribution:

$$\tau_{xx} = \Gamma e^{-2z\phi + 2c_1} + c_3 e^{-(\alpha/De)\phi} \quad \text{with} \quad \Gamma = -2z \frac{De B^2 \alpha^2}{Re(\alpha - 2z De)} \tag{11}$$

The first term on the right-hand side of Eq. (11) is $\Gamma \tau_{xy}^2$, whereas the second term must vanish when $t \rightarrow \infty$. In the absence of suction/blowing, this particular boundary condition helps to define the general quantities A and B introduced early in this section.

At the wall the general velocity profile of Eq. (8) only has a real component and it must be consistent with the no-slip condition. Hence, at $y = 0$ this equality gives

$$\frac{B}{Re\,(A + v_w B)}\, e^{c_1}\, e^{-zAt} = e^{it} \tag{12}$$

from which two results are obtained: (1) the constant of integration c_1

$$c_1 = \ln\left[\frac{Re\,(A + v_w B)}{B}\right] \tag{13}$$

and (2) the equality $-zA = i$

$$-zA = i \rightarrow \frac{-A}{De\,(A + v_w B) - \left(B^2/Re\,(A + v_w B)\right)} = i. \tag{14}$$

This is an algebraic second-order equation on B, that can be solved to give two possible solutions for B.

$$B = \frac{A v_w Re\,(i - 2De) + mAi\sqrt{Re}\sqrt{v_w^2 Re + 4\,(i - De)}}{2\left(v_w^2 De\, Re - 1\right)} \quad \text{with}$$

$$m = \pm 1 \tag{15-a}$$

It is clear that there is a singularity when $v_w^2 De\, Re = 1$ (this corresponds to $M_w = \pm 1$). For this particular viscoelastic case, Eq. (14) turns out to be linear on B and its solution is

$$B = \frac{-A\,(1 - i\,De)\,(1 + i2\,De)}{v_w^*\left(1 + i4De^2\right)} \tag{15-b}$$

where $v_w = v_w^* = \pm 1/\sqrt{De\, Re}$ or, alternatively using the other set of non-dimensional numbers $(M,\ E,\ M_w)$, $B = \left(-AM\left(1 - iM\sqrt{E}\right)\left(1 + i2M\sqrt{E}\right)\right)/\left(M_w^*\left(1 + i4M^2 E\right)\right)$ and $M_w = M_w^* = \pm 1$. The asterisk is used to denote the critical value.

Given the definition of ϕ and that the velocity must vanish as $y \rightarrow \infty$, it is necessary for the real part of the exponential appearing in the velocity profile (Eq. (8)) to be negative $-(zB)_{real} < 0$. Given the expressions above, and after some laborious mathematics carried out with MATHEMATICA v5 from Wolfram Research, the real and imaginary parts of $-zB$ are given by Eqs. (16-a) and (16-b), respectively. This is for the general case where $v_w^{*2} De\, Re \neq 1$ (or $M_w \neq \pm 1$).

$$(-zB)_{real} = \frac{\left\{v_w Re\, a_1 + \sqrt{Re}\,\varphi^{1/4}\,[a_2 + a_3 + a_4]\right\}}{\left(v_w^2 Re\, De - 1\right)[a_5 + a_6 + a_7]} \tag{16-a}$$

$$(-zB)_{imag} = \frac{-i\sqrt{Re}\left\{m\left(1 + v_w^2 Re\, De\right)a_8 + v_w\sqrt{Re}\,(a_9 + a_{10} + a_{11})\right\}}{\left(v_w^2 Re\, De - 1\right)(a_5 + a_6 + a_7)} \tag{16-b}$$

where

$$\varphi = v_w^4 Re^2 - 8v_w^2 Re\, De + 16\left(1 + De^2\right)$$

$$\theta = \mathrm{Arg}\left[v_w^2 Re - 4De + 4i\right] = \arctan\left(\frac{4}{v_w^2 Re - 4De}\right)$$

with functions a_1 to a_{11} given below.

$$a_1 = -8 + v_w^2 Re\left(v_w^2 Re + 4De - 2\sqrt{\varphi}\right)$$

$$a_2 = -2m v_w^2 Re\left(v_w^2 Re + \sqrt{\varphi}\right)\cos\left(\frac{\theta}{2}\right)$$

$$a_3 = -v_w^3 Re^{3/2}\varphi^{1/4}\cos\theta$$

$$a_4 = -\left(1 + v_w^2 Re\, De\right)$$
$$\times \left[m\left(v_w^2 Re - 4De + \sqrt{\varphi}\right) + 2v_w\sqrt{Re}\,\varphi^{1/4}\cos\left(\frac{\theta}{2}\right)\right]\sin\left(\frac{\theta}{2}\right)$$

$$a_5 = v_w^4 Re^2 + 8 + 16De^2 + 2v_w^2 Re\sqrt{\varphi}$$

$$a_6 = 2m v_w\sqrt{Re}\left(v_w^2 Re + 4De + \sqrt{\varphi}\right)\varphi^{1/4}\cos\left(\frac{\theta}{2}\right)$$

$$a_7 = \left(v_w^2 Re + 4De\right)\sqrt{\varphi}\cos\theta$$

$$a_8 = \left(3v_w^2 Re + 4De + \sqrt{\varphi}\right)\varphi^{1/4}\cos\left(\frac{\theta}{2}\right)$$

$$a_9 = \left(1 + v_w^2 Re\, De\right)\left(v_w^2 Re + 4De + 2\sqrt{\varphi}\right)$$

$$a_{10} = \left(1 + v_w^2 Re\, De\right)\sqrt{\varphi}\cos\theta$$

$$a_{11} = 4De\,\varphi^{1/4}\left[2m v_w\sqrt{Re}\sin\left(\frac{\theta}{2}\right) + \varphi^{1/4}\sin\theta\right]$$

For the specific case of $v_w^{*2} De\, Re = 1$ (or $M_w = M_w^* = \pm 1$), the solutions of $(-zB)_{real}$ and $(-zB)_{imag}$ are given by

$$(-zB)_{real} = \frac{\sqrt{E}M^2}{M_w^*\left(1 + 4EM^2\right)} \tag{16-c}$$

$$(-zB)_{imag} = \frac{M\left(1 + 2EM^2\right)}{M_w^*\left(1 + 4EM^2\right)} \tag{16-d}$$

It is now possible to back-substitute some of the above equations to obtain the final expressions for the velocity and stress fields. For the velocity, the final equation takes the form

$$u = e^{-z\phi} \rightarrow u = e^{-z(At + By)} \rightarrow u = e^{(-zB)_{real}y}\, e^{i\left[t + (-zB)_{imag}y\right]} \tag{17}$$

where $e^{i\left[t + (-zB)_{imag}y\right]} = \cos\left[(-zB)_{imag}y + t\right]$ and $(-zB)_{real}$ and $(-zB)_{imag}$ are given by Eqs. (16-a) and (16-b) for $M_w \neq 1$ and by Eqs. (16-c) and (16-d) for $M_w = 1$, respectively.

The condition $(-zB)_{real} < 0$ clarifies which of the two possible solutions of Eq. (15-a) exists. Only the solution for $m = -1$ obeys this condition for Newtonian flows and UCM flows with suction. For UCM flows with blowing $m = -1$ always provides a physically realistic solution, but for $M_w > 1$ the $m = +1$ solution is also physically possible leading to negative values of $(-zB)_{real}$. In this case, the velocity profile of Eq. (17) must be substituted by a linear combination of the two solutions, a matter to be discussed in Section 4.4.

The stress field results from substituting the velocity field solution into Eqs. (7) and (11) for the xy and xx components, respectively. The corresponding expressions are given in Appendix B.

4. Results and discussion

Some results of the previous section are discussed in detail here to investigate the role of the various relevant independent non-dimensional numbers. It starts with the revisit of the Newtonian case and of the viscoelastic solution in the absence of cross flow after which the new results of this work are presented. First, the investigation of the viscoelastic flow with suction for low and large viscoelastic Mach numbers for which there is a limit when the suction velocity equals the elastic wave speed ($M_w = -1$). This is

followed by results with blowing through the porous plate, which does not suffer from the same limitation, but leads to a richer set of solutions including chaotic-like behavior under some conditions.

To help analyze and interpret the results two important quantities are defined: y_c is the normalized peak-to-peak distance of two consecutive oscillations and y_p is the normalized penetration depth, measuring the penetration of the oscillating wave. This is the distance from the plate to the location where the maximum amplitude of oscillation has been reduced to 1% of the amplitude of oscillation of the plate, so it is equivalent to a boundary layer thickness. These quantities are given by Eqs. (18) and (19), respectively.

$$y_c = \frac{2\pi}{(-zB)_{imag}} \quad (18)$$

$$y_p = \frac{-\ln(0.01)}{(-zB)_{real}} = \frac{4.6}{(-zB)_{real}} \quad (19)$$

With the characteristic time ($t_c = 2\pi/\omega$) of the plate oscillation the velocity of penetration of the wave (V_p) can also be determined as the ratio between the peak-to-peak distance and the characteristic time scale, as given by Eq. (20).

$$V_p = \frac{y_c}{t_c} \rightarrow V_p = \frac{U_0}{(-zB)_{imag}} \quad (20)$$

4.1. Newtonian flow with a porous oscillating wall

Fig. 1 presents velocity profiles for Newtonian fluids to assess the combined effects of transverse velocity and Reynolds number in the absence of elasticity. These include the situation with no cross flow of Stokes [10] and Lord Rayleigh [11]. All the profiles shown here and henceforth correspond to the moment when the oscillating plate is at the maximum amplitude of oscillation. Fig. 1a is for suction, whereas Fig. 1b concerns blowing. For small suction velocities ($|v_w| \leq 0.01$) the profiles of stream-wise velocity are unaffected by suction. As suction strengthens the penetration depth decreases, the stream-wise velocity profiles approach the plate and the amplitude of fluid oscillation away from the plate is also reduced. This decrease of the amplitude of oscillation is due to the development of larger stream-wise shear stresses when suction brings the oscillating layers of fluid close to each other and to the plate, increasing the velocity gradients. However, the peak-to-peak distance y_c increases and consequently the ratio y_p/y_c decreases faster than the penetration depth as can be seen on the left-half of Fig. 2a. Note that suction velocities are negative and blowing velocities are positive.

For weak injection, the stream-wise velocity profiles are also identical to the profile for an impermeable wall. As the blowing velocity is raised, the penetration depth increases, fluid is pushed away from the wall and the amplitude of the oscillations of the fluid layers away from the wall also increase, i.e., blowing has the opposite effect of suction. This is also clear from inspection of the right-half of Fig. 2a, where both the peak-to-peak distance and the ratio y_p/y_c increase with blowing velocity, showing the opposite trends to those depicted on the left-side of the graph pertaining to suction.

To understand the effect of Reynolds number on the plot of u/U_0 versus $y\omega/U_0$ one is reminded that an increase in Reynolds number requires an increase in the amplitude of the oscillation, a decrease in its frequency or both (not to mention viscosity), i.e., the ordinate of the plot, $y\omega/U_0$, decreases and the waves become compressed towards the plate, leading to higher shear rates and in spite of the reduction in the amplitude of the waves away from the wall.

At $Re = 1$ the effect of the oscillating plate penetrates visibly to as much as $y = 8$, but for suction this is significantly reduced on increasing the Reynolds number (at $Re = 10$ the fluid is almost at
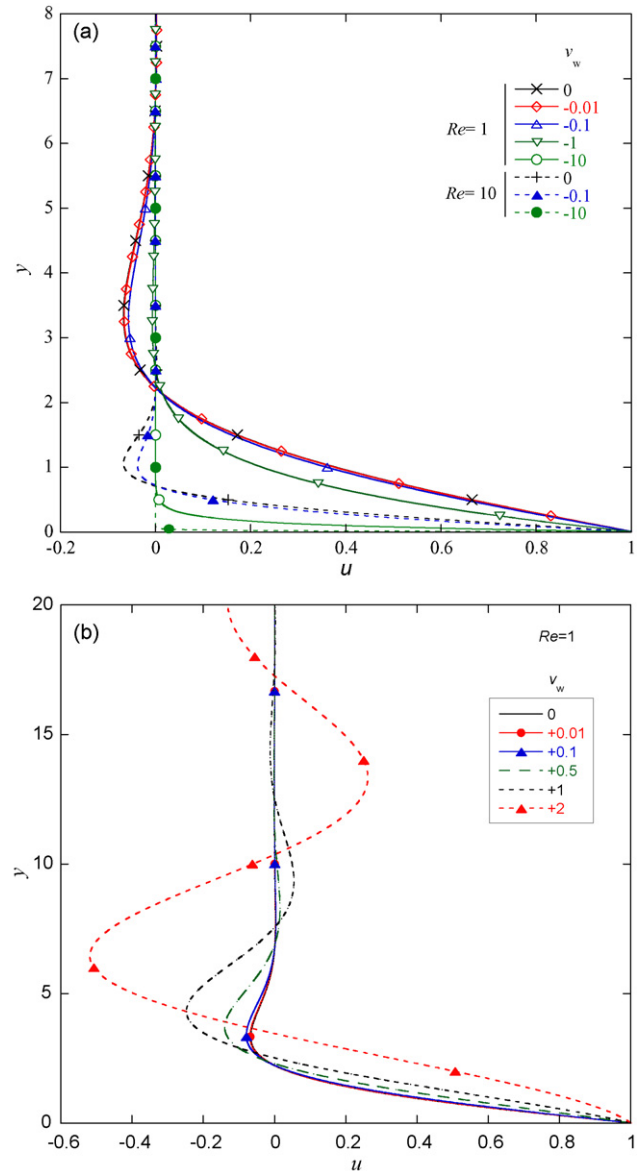

Fig. 1. Influence of Reynolds number and velocity through the porous wall on the profiles for Newtonian fluids: (a) Suction with $Re = 1$ and $Re = 10$; (b) Injection with $Re = 1$.

rest at $y = 3$, cf. Fig. 1a), i.e., the penetration depth decreases on inverse proportion to Re. With blowing the opposite is true with the penetration depth increasing with cross flow velocity (cf. Fig. 2a). The variation of y_p with Reynolds number is non-linear due to the effect of the cross flow velocity. This variation is by a factor of 3 at $v_w = 0$ rising to a factor of 10 as the cross flow velocity tends to infinity, regardless of whether there is suction or blowing.

In contrast to y_p and y_p/y_c the variation of the peak-to-peak distance with v_w plotted in Fig. 2b has a non-monotonic behavior and depends only on the magnitude of the cross flow velocity. It is symmetric with the minimum value attained for the impermeable wall. At large cross flow velocities y_c becomes independent of the Reynolds number. For suction y_c is always larger than the penetration depth, so only a single cycle, or part of it is actually seen in Fig. 1. At both $v_w = 0$ and infinite suction y_p/y_c becomes independent of the Reynolds number.

The Reynolds number effect with blowing is similar to the effect for suction, but for conciseness no further plot is shown for this
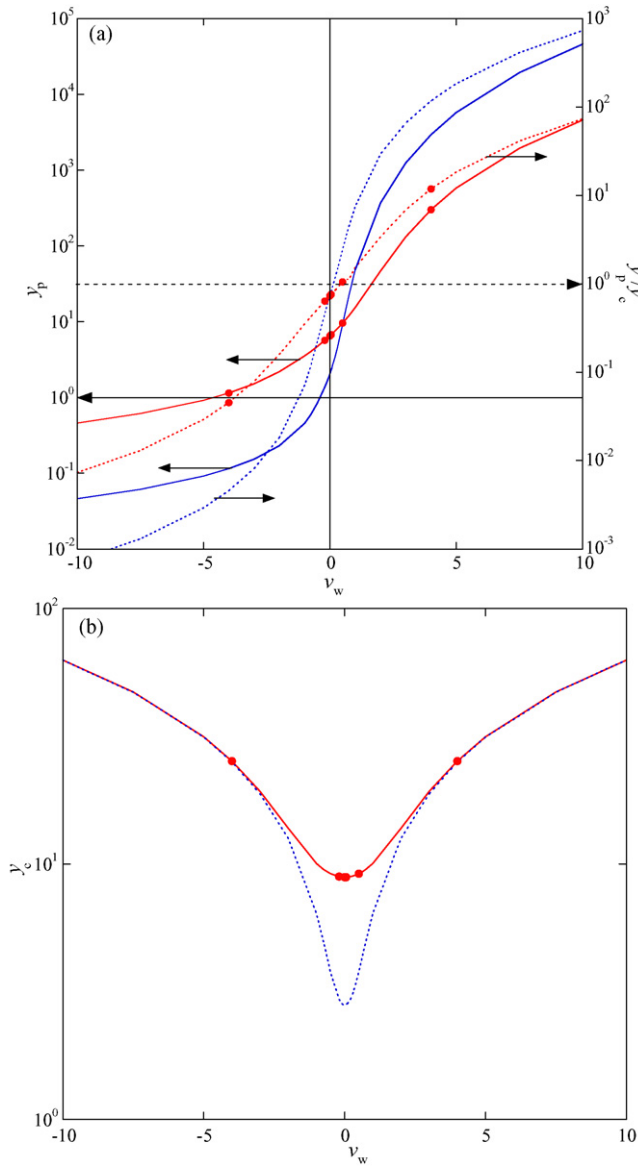
Fig. 2. Variation of normalized penetration depth (y_p) and of y_p/y_c with cross flow velocity for Newtonian fluids (red and circles (Re = 1), blue (Re = 10)): (a) penetration depth (y_p) (full lines) and of y_p/y_c (dashed lines); (b) peak-to-peak distance (y_c). (For interpretation of the references to color in this figure legend, the reader is referred to the web version of the article.)

case. The shear stress profiles are in agreement with the corresponding velocity profiles of Fig. 1 as far as the effects of Re and v_w are concerned, taking into account that they are proportional to the velocity gradient, and again they are not shown here for conciseness.

4.2. Viscoelastic flow with an impermeable oscillating wall

The second reference case pertains to flow of viscoelastic fluids without cross flow, the solution of which can be found elsewhere [3,4]. Representative stream-wise velocity profiles at Reynolds numbers of 1 and 10, and showing the effects of Deborah number, are plotted in Fig. 3. For $De \leq 0.01$, cases here corresponding to $M \ll 1$, there are hardly detectable differences relative to the Newtonian profiles. On increasing the Deborah number, or elastic Mach number, two different characteristics become obvious. First, the shape of the velocity profile progressively evolves from that of a
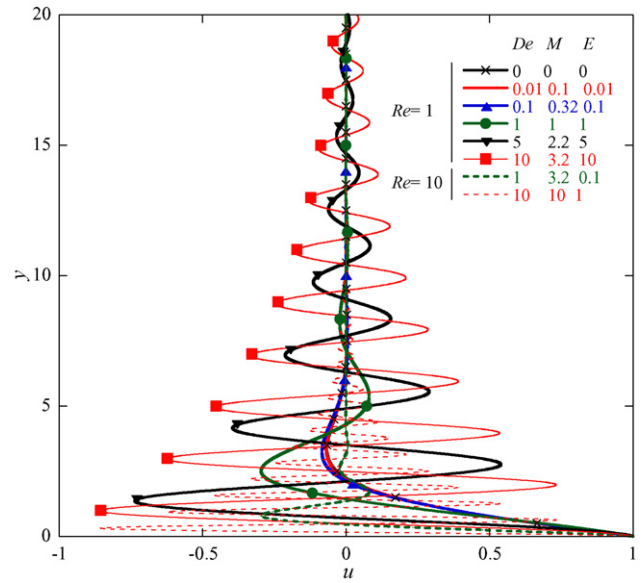

Fig. 3. Influence of Reynolds and Deborah numbers on the velocity profiles in the absence of suction/injection at Re = 1 and 10.

diffused wave at low elastic Mach numbers towards a less dampened wave (elastic wave) containing more and more visible cycles at large Mach numbers (or large Deborah numbers). At low Reynolds numbers, as for Re = 1 in Fig. 3, it looks as though this change of behavior is associated with the transition from sub-critical to super-critical flow (M = 1 defining the critical condition), but inspection of data for Re = 10 shows that the elastic Mach number is not the critical parameter (the curve for M = 1 at Re = 1 looks like the curve for M = 3.2 at Re = 10 in spite of the ordinate difference). Inspection of Fig. 4, where penetration-depth related quantities $y_p\sqrt{Re}$ and y_p/y_c are plotted as a function of Deborah number, as for Newtonian fluids, shows that both quantities are independent of Reynolds
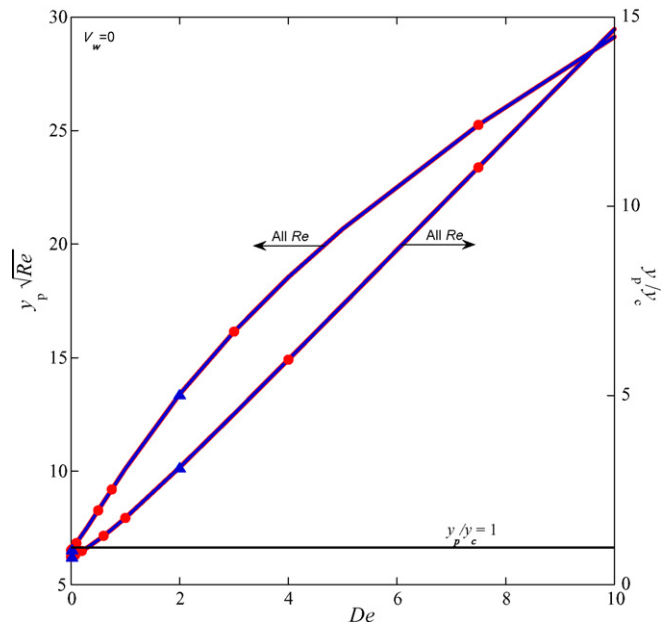

Fig. 4. Variation of characteristic length scales $y_p\sqrt{Re}$ and y_p/y_c with Deborah number in the absence of suction: red lines and circles Re = 1; blue lines and triangles Re = 10. (For interpretation of the references to color in this figure legend, the reader is referred to the web version of the article.)

number in the absence of cross flow, and only depend on the Deborah number. The dependence of y_p/y_c on De is non-linear only at low De and becomes linear at $De \geq 1$. The dependence on the Reynolds number is identical to that seen for Newtonian fluids as it should be because the momentum equation is linear in the absence of cross flow (as well as at constant cross flow velocity). It follows from dimensional analysis (PI theorem) that u/U_0 is a function of $y/\sqrt{t\nu}$ from which the $\sqrt{Re}$ dependence issues.

On increasing De, the amplitude of the oscillating wave is also progressively less dampened on moving away from the plate and consequently the penetration depth of the wave increases. Simultaneously, the shear wave speed and the peak-to-peak distance (y_c) of the traveling wave decrease with De and more and more cycles become visible in Fig. 3.

This is consistent with the definition of the shear wave speed in a fluid at rest $c = \sqrt{\eta/(\rho\lambda)} = U_0/M = U_0/\sqrt{Re\,De}$, which decreases as the Mach or Deborah numbers rise. The fluid velocity is normalized by the amplitude of the velocity oscillation at the plate, so any change in this amplitude should not affect the plotted velocity, other factors being equal. The waves become more persistent and the wave propagation speed decreases on account of elasticity and this is well seen in the increase of $y_p\sqrt{Re}$ with De shown in Fig. 4. However, in contrast to the impact of cross flow of the previous sub-section, the Deborah number does not change the impact of Reynolds number in a non-linear manner. The plot of $y_p\sqrt{Re}$ versus De in Fig. 4 collapses the penetration data pertaining to different Reynolds numbers. The same happens with the peak-to-peak distance and that explains the Reynolds number independence of y_p/y_c.

4.3. Viscoelastic flow with suction through the porous oscillating wall

As for Newtonian fluids, the solutions to this case require $m = -1$ in Eq. (15-a), whereas $m = +1$ implies physically unrealistic solutions.

The two plots of Fig. 5 are for a constant Reynolds number of 1 and Deborah numbers of 0.01 and 1, respectively. Within each plot the suction velocity is varied, but no solution is ever obtained when the suction velocity exceeds the wave speed, i.e. for $|M_w| > 1$. When the suction velocity equals the wave speed ($M_w = -1$) only the fluid particles attached to the plate move in the stream-wise direction and elsewhere the stream-wise velocity is zero (but not the normal velocity $v = v_w$).

Fig. 5a pertains to subcritical Mach numbers ($M < 1$) and Fig. 5b is for $M = 1$. The effects of Deborah number are those expected from the findings of the previous section, but now combined with suction effects. Accordingly, the stream-wise velocity profiles are dampened very quickly on moving away from the wall and the stream-wise velocity vanishes essentially after one full period of oscillation. For $M = 1$ (higher De), the amplitude of the oscillation is stronger and at $y = 10$ the oscillation is weak, but still visible. The reduction in the rate of decrease of the amplitude of oscillation with suction due to increases in fluid elasticity is especially well shown in comparisons between Fig. 5a and Fig. 5b. In Fig. 5b more than one cycle is visible because the waves are less dissipative than in Fig. 5a.

The plot of Fig. 6 pertains to a higher Reynolds number of 10 and a Deborah number of 10 corresponding to a hypercritical elastic Mach number ($M > 5$). The wave behavior is now largely dominated by fluid elasticity rather than by viscous effects with several cycles in evidence especially when suction is weak. For conciseness, profiles at lower Deborah numbers and $Re = 10$ are not shown since they are similar to those of Fig. 5, even though they are closer to
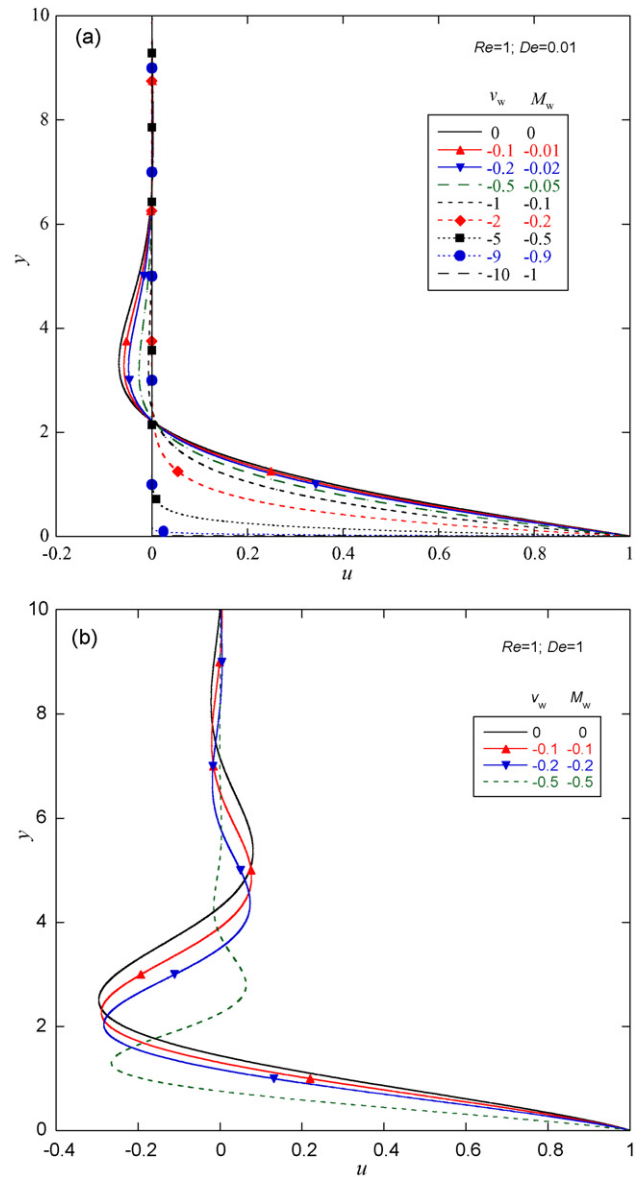

Fig. 5. Effect of suction velocity through the porous plate on the velocity profiles for $Re = 1$: (a) $De = 0.01$ ($M = 0.1$ and $E = 0.01$); (b) $De = 1$ ($M = 1$ and $E = 1$).

the wall on account of the Reynolds number effect. As for $Re = 1$, $M_w = -1$ marks the limit of physical solutions.

The variations of the penetration depth and ratio y_p/y_c with the elastic suction Mach number are plotted for $Re = 1$ and $Re = 10$ in Fig. 7a and b, respectively, as a function of Deborah and Reynolds numbers. Their variations with M_w are non-linear at low Deborah number and tending to linear as the Deborah number increases and the flow becomes dominated by elasticity. As for viscoelastic flow in the absence of cross flow, Fig. 7a and b confirms that the penetration depth and the peak-to-peak distance continue to scale with $1/\sqrt{Re}$ even in the presence of combined effects of elasticity and suction as it should be from the linearity of the momentum equation and dimensional analysis arguments. For conciseness only $y_p\sqrt{Re}$ is plotted in Fig. 7a. The change of wave behavior from liquid-like to solid-like is well shown in the variations of y_p/y_c with De plotted in Fig. 7b. At low Deborah numbers, as for Newtonian fluids, the peak-to-peak distance is larger than the penetration depth ($y_p/y_c < 1$), but this ratio increases significantly with De leading to $y_p/y_c > 1$, corresponding to more visible cycles as seen in Fig. 6. As De increases the
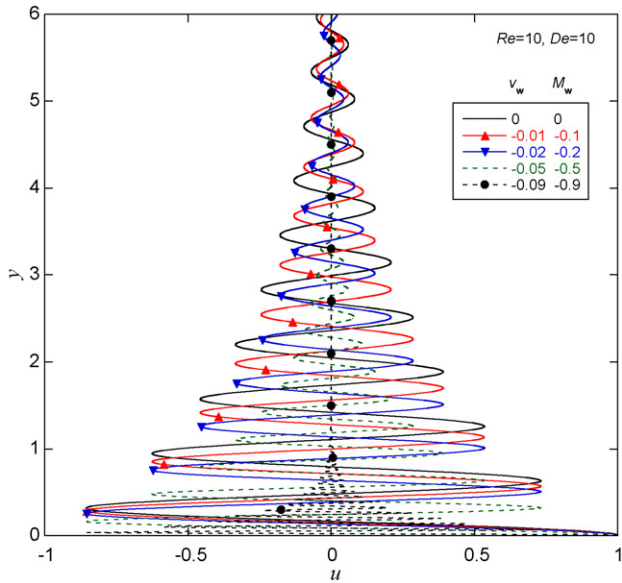
Fig. 6. Effect of suction velocity through the porous plate on the velocity profiles for hypercritical elastic Mach numbers ($Re = 10$ and $De = 10$ ($M = 10$ and $E = 1$)).

flow characteristics also become progressively independent of the amount of suction. At $M_w = -1$ it is clear that $y_p/(y_c \times De)$ attains a constant value of 14.64. So, even though the analytical solution is somewhat complex, this complex viscoelastic flow still follows simple scaling laws.

4.4. Viscoelastic flow with blowing through the porous oscillating wall

In contrast to suction, with injection through the porous plate the physical solutions are not limited to sub-critical elastic Mach numbers ($M_w < 1$) and three distinct flow regimes are observed as investigated below.

For sub-critical conditions there is still a single physically correct solution, which corresponds to $m = -1$ in Eq. (15-a). The $m = +1$ solution violates the boundary condition (4-b), which imposes that only negative values of $(-zB)_{real}$ are valid. In these cases the velocity profiles plotted are still given by Eq. (17).

However, for super-critical conditions $m = +1$ also implies $(-zB)_{real} < 0$ and the profiles plotted now correspond to the linear combination of the two possible solutions of Eq. (21) ($m = \pm 1$) together with the boundary condition (4-a). This is so because a linear combination of the two solutions is also a solution and this is carried out introducing parameter c_3.

$$u = c_3 e^{-z\phi_+} + (1 - c_3)e^{-z\phi_-} \tag{21}$$

Here, to investigate the relevance of the $m = -1$ and $m = +1$ contributions the coefficient c_3 is assumed to be 0.5 to equally consider the influence of each solution to u.

At hypercritical conditions, and even though there are still two analytical solutions, the solution for $m = -1$ dominates the flow as will be shown in Section 4.4.2.

4.4.1. Sub-critical elastic injection Mach number flow

Fig. 8a and b shows transverse profiles of the stream-wise velocity for Reynolds numbers of 1–10 at various Deborah numbers, all cases pertaining to sub-critical injection elastic Mach numbers ($M_w < +1$). The effect of blowing is opposite to that seen in the previous sub-section for suction. The penetration depth of the oscillations, its wavelength and amplitude increase with M_w, while wave
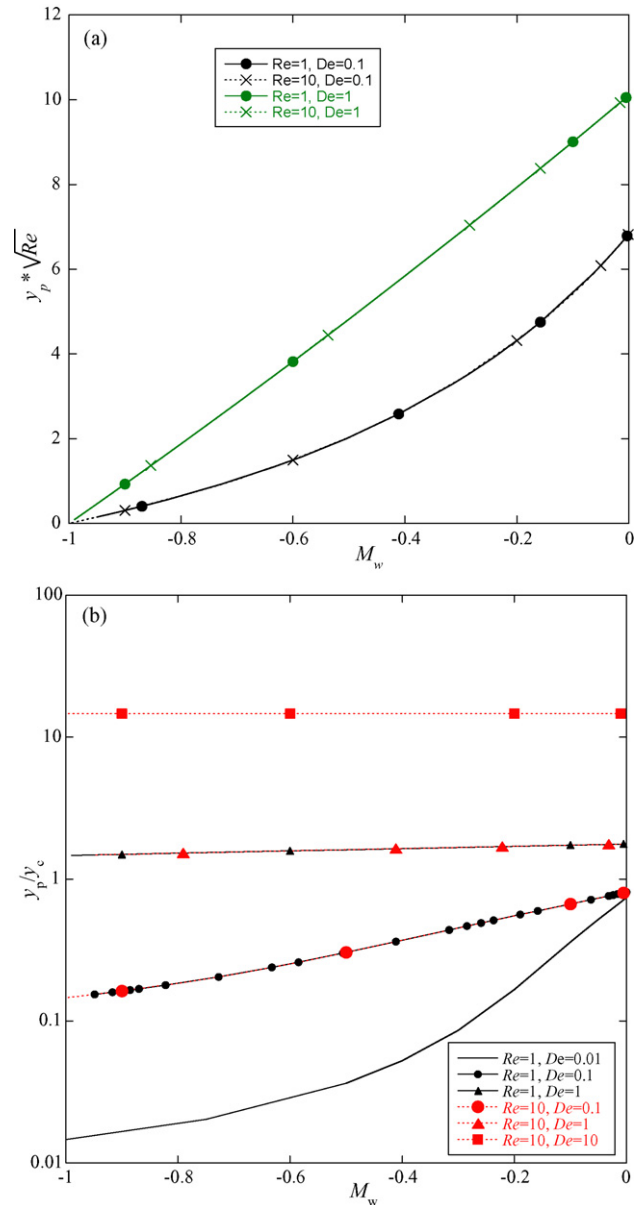

Fig. 7. Variation of characteristic lengths with suction elastic Mach number as a function of Deborah and Reynolds numbers: (a) $y_p\sqrt{Re}$; (b) y_p/y_c.

dampening becomes less pronounced with more complete cycles visible. This effect is especially strong when M_w approaches the critical value of +1.

The comparisons between the plots of Fig. 8a–c shows complex non-monotonic effects of Deborah and viscoelastic injection Mach numbers, which are summarized in the penetration depth plots of Fig. 9. As previously seen with suction and without cross-flow, the use of $\sqrt{Re}$ collapses data as far as Reynolds number effects are concerned. At low Deborah numbers (say, $De = 0.01$), the cross flow strongly enhances the amplitude of the oscillations in a non-linear way and strongly reduces the dampening effects of viscous shear stresses by pushing fluid away from the wall and consequently lowering the shear rates, thus making more cycles visible. On increasing the Deborah number the cross flow still enhances the amplitude of the oscillations, but by a lesser amount and the variations with M_w become more linear (cf. Fig. 9). The amplitude of the velocity profiles at $M_w \approx 0.5$ for $De = 0.1$ are not as large as for $De = 0.01$ in
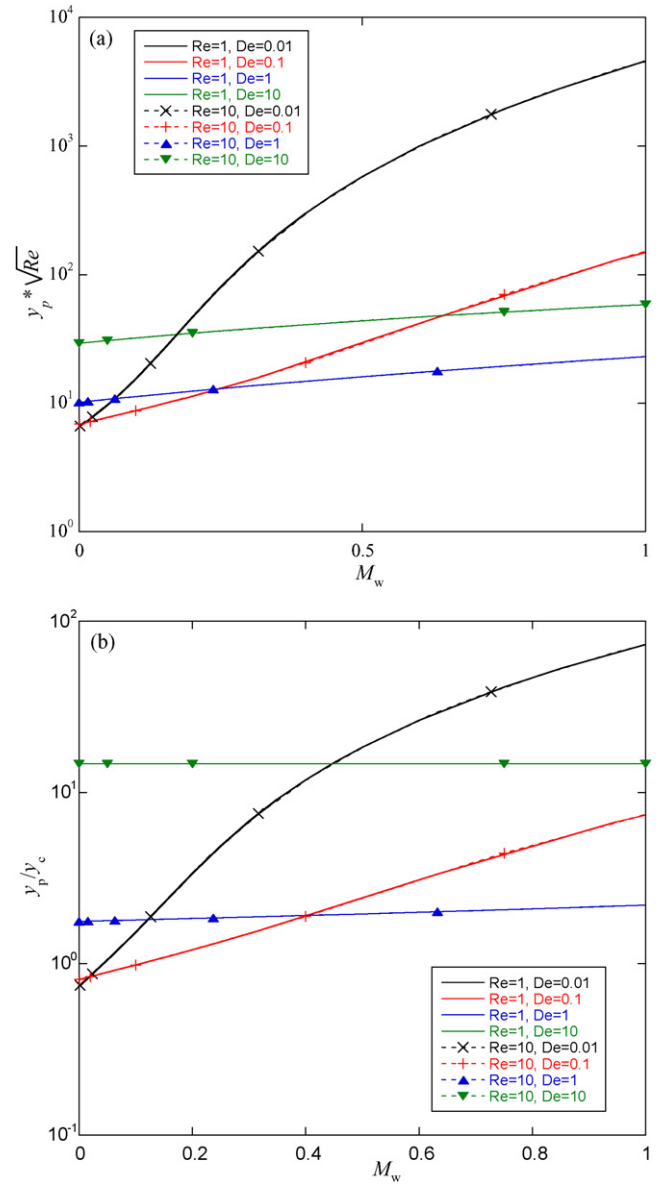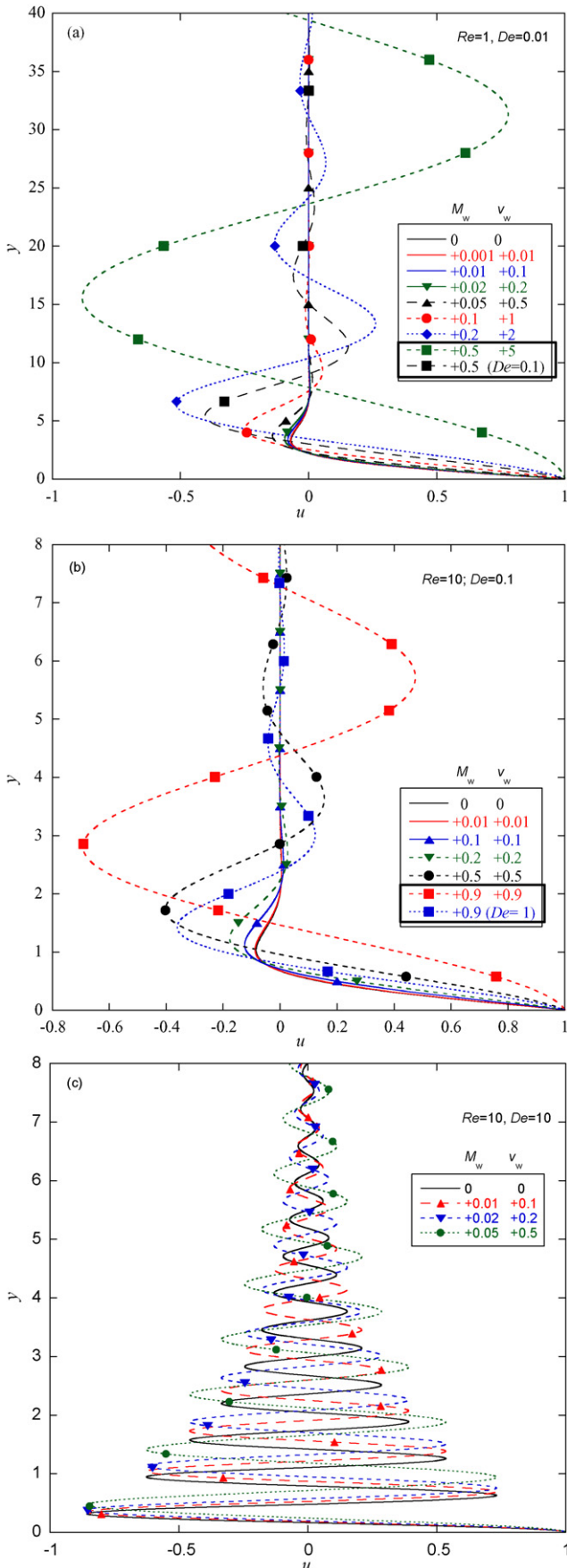
Fig. 9. Variation of characteristic lengths as a function of Deborah number and the viscoelastic injection Mach number under the sub-critical injection conditions: (a) $y_p\sqrt{Re}$; (b) y_p/y_c.

Fig. 8a and b. So, at low Deborah numbers the flow characteristics are essentially dominated by the injection (M_w).

Further increasing the Deborah number to 1 and 10, makes elasticity dominate the flow and the variations of the flow characteristics with M_w weaken. In particular, the variations of the penetration depth and the peak-to-peak distance in Fig. 9 become identical, leading to constant y_p/y_c that are independent of M_w at large De. At very low values of M_w the velocity profiles at high De have more cycles than at lower De (cf. Fig. 8b and c), because of the more solid-like nature of the waves, but on increasing M_w the changes are small (cf. Fig. 8c).

Fig. 8. Effect of injection velocity through the porous plate on the velocity profiles for sub-critical injection elastic Mach numbers ($M_w < 1$): (a) $Re = 1$, $De = 0.01$ ($M = 0.1$ and $E = 0.01$) and $De = 0.1$ ($M = 0.32$ and $E = 0.1$); (b) $Re = 10$, $De = 0.1$ ($M = 1$ and $E = 0.01$) and $De = 1$ ($M = 3.2$ and $E = 0.1$); (c) $Re = 10$, $De = 10$ ($M = 10$ and $E = 1$).
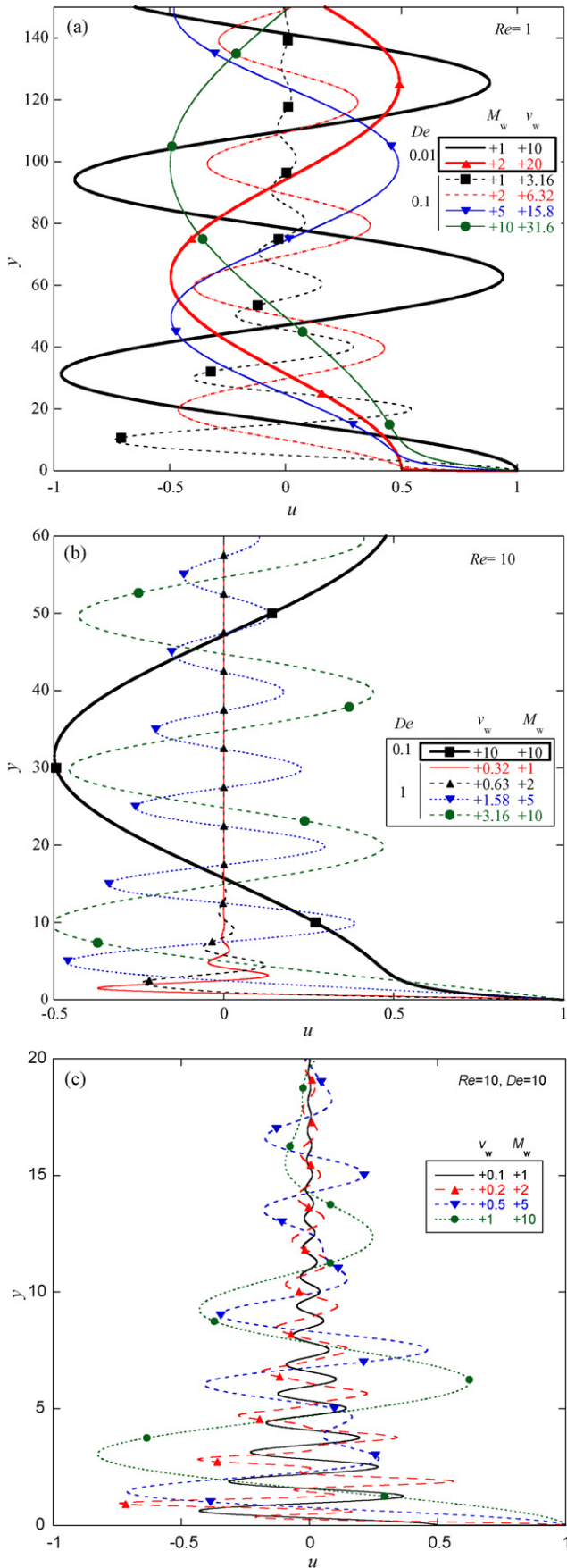
It is this large effect of M_w at low De and the small effect of M_w at high De that results in the non-monotonic variations observed under sub-critical conditions well illustrated in Fig. 9. This complex behavior already contrasts with the monotonic variations seen when the cross-flow originates from suction at the porous plate. Nevertheless, the sub-critical flow with blowing is well-behaved in the sense that the solution of Eq. (15-a) is unique with $m = -1$.

4.4.2. Critical and super-critical elastic injection Mach numbers

Fig. 10a and b presents transverse profiles of stream-wise velocity for critical ($M_w = 1$) and supercritical ($M_w > 1$) elastic injection Mach numbers corresponding to the same Reynolds and Deborah numbers of Fig. 8a–c. These velocity profiles represent Eq. (21) and correspond now to the sum of the two possible solutions for $m = \pm 1$, but first we look at the variations of the penetration depth ($y_p^{\pm} \sqrt{Re}$) and peak-to-peak distance ($y_p^{\pm}/y_c^{\pm}$) with M_w as a function of De and Re and using log–log coordinates. For $m = -1$, data from the sub-critical M_w region is included. Starting with $m = -1$ we observed that log ($y_p^{-} \sqrt{Re}$) and log (y_p^{-}/y_c^{-}) tended to constant values when $M_w \to 0$ (a minus superscript indicates $m = -1$), whereas when M_w grew beyond 1 the log–log variations were linear with equal slopes and separations suggesting that in this region $y_p^{-} \sqrt{Re}$ and y_p^{-}/y_c^{-} scale uniquely with $M_w/\sqrt{De}$, as shown in Fig. 11a and b.

For $m = +1$, (log $\left(y_p^{+} \sqrt{Re}\right)$) grows linearly at large log (M_w) also with equal slopes and separations, but now at equal values of M_w, higher values of $y_p^{+} \sqrt{Re}$ correspond to higher values of De in clear contrast to the behavior for $m = -1$. This indicates that at large M_w, $y_p^{+} \sqrt{Re}$ now scales uniquely with $M_w \sqrt{De}$, as shown in Fig. 11c, rather than with $M_w/\sqrt{De}$ as was the case for $m = -1$. Indeed, looking at the limiting behaviors of y_p^{+} and y_p^{-} for $M_w \to +\infty$ give the results of Eq. (22), which are consistent with the plots. These equations also explain the three times larger slope of $y_p^{-} \sqrt{Re}$ versus $M_w/\sqrt{De}$ of Fig. 11a in relation to the slope of $y_p^{+} \sqrt{Re}$ versus $M_w \sqrt{De}$ in Fig. 11c at large Deborah numbers. At even larger values of $M_w/\sqrt{De}$ the slope difference would be by a factor of 4.

$$\lim_{M_w \to +\infty} y_p^{+} \propto \frac{M_w \sqrt{De}}{\sqrt{Re}} \tag{22-a}$$

$$\lim_{M_w \to +\infty} y_p^{-} \propto \frac{M_w^3}{De^{3/2}\sqrt{Re}} + \frac{M_w^4}{4De\,(1+De)\,\sqrt{Re}} \tag{22-b}$$

However, the curves for $De = 10$ in Fig. 11c only seem to comply with these findings at very large values of M_w and show an intermediate behavior at lower M_w. The reasons for this will be explained shortly.

The behavior of log $\left(y_p^{+}/y_c^{+}\right)$ contrasts with all others and in particular with that of log $\left(y_p^{-}/y_c^{-}\right)$ in Fig. 11b in the sense that y_p^{+}/y_c^{+} is almost constant for each value of De and consequently it does not scale with $M_w \sqrt{De}$. Instead, the correct scaling is $\left(y_p^{+}/y_c^{+}\right)/De$ versus M_w as shown in Fig. 11d. This figure shows again the existence of a large deviation in the behavior of the $De = 10$ curve, which already affects the curve at $De = 1$, but to a lesser extent. Indeed, plotting $\left(y_p^{+}/y_c^{+}\right)/De$ in the range $1 \le De \le 10$ in Fig. 11d as long dashes, shows a progressive variation of $\left(y_p^{+}/y_c^{+}\right)/De$ in this range, which explains the apparent discrepancy of the $De = 10$ data in Fig. 11c. To understand this phenomenon the asymptotic behavior of y_p^{+} was derived when De grows to infinity but M_w is kept constant (or $v_w \to 0$ at constant Re). The result is given in Eq. (23) and confirms

Fig. 10. Effect of injection velocity through the porous plate on the velocity profiles for critical and supercritical injection elastic Mach numbers ($M_w \ge 1$): (a) $Re = 1$, $De = 0.01$ ($M = 0.1$ and $E = 0.01$) and $De = 0.1$ ($M = 0.32$ and $E = 0.1$); (b) $Re = 10$, $De = 0.1$ ($M = 1$ and $E = 0.01$) and $De = 1$ ($M = 3.2$ and $E = 0.1$); (c) $Re = 10$, $De = 10$ ($M = 10$ and $E = 1$).
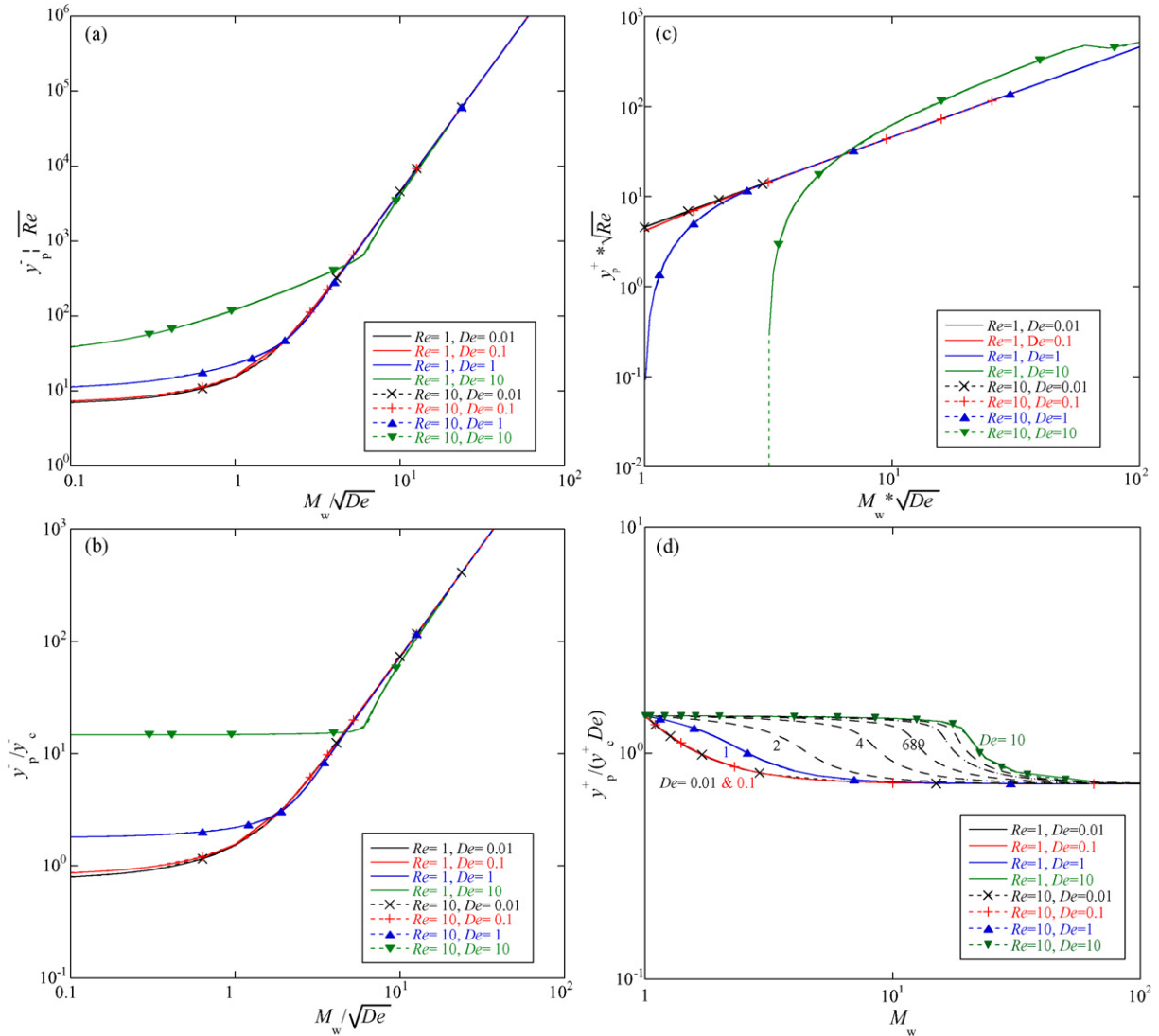
Fig. 11. Variation of characteristic lengths for critical and super-critical injection conditions: (a) $y_p^- \sqrt{Re}$ versus $M_w/\sqrt{De}$; (b) y_p^-/y_c^- versus $M_w/\sqrt{De}$; (c) $y_p^+ \sqrt{Re}$ versus $M_w \times \sqrt{De}$; (d) y_p^+/y_c^+ versus M_w.

that when both De and M_w are large, $y_p^+ \sqrt{Re}$ varies with $M_w \sqrt{De}$. At intermediate values the fast variations are the outcome of the large powers of De and M_w.

$$\lim_{De \to +\infty} y_p^+ \propto \frac{\sqrt{De} \left(32De^4 M_w + 16De^2 M_w^3 + M_w^5\right)}{\sqrt{Re} \left(4De^2 + M_w^2\right) \left(4De^2 + 4De^2 M_w + M_w^2\right)} \quad (23)$$

The variations of the stream-wise velocity profiles with M_w, De and Re of Fig. 10a–c have similarities to those seen in the sub-critical regime, where the two different behaviors at low and high De were identified and are easy to interpret by looking also at Fig. 11a. When De is very low and injection dominates flow characteristics, an increase in M_w increases the amplitude of oscillations, with concomitant variations in its wavelength. As the Deborah number is increased, but still in the region of Fig. 11a where the $\log\left(y_p^- \sqrt{Re}\right)$ versus $\log\left(M_w/\sqrt{De}\right)$ is not yet a straight line, the amplitude of oscillations is lower at the same value of M_w than at lower De. Now the effect of M_w has been reversed, because elastic effects start to take control of flow characteristics and the amplitude of oscillations start decreasing with an increase in M_w. In this intermediate region

where $\log\left(y_p^- \sqrt{Re}\right)$ versus $\log\left(M_w/\sqrt{De}\right)$ is non-linear, a chaotic-like behavior starts to be observed for some cases provided $M_w > 1$, as will be discussed.

In Fig. 10a an unusual behavior of the velocity profiles in the near wall region is already perceptible and this represents the beginning of the chaotic-like behavior discussed in the next section. Here, this is caused by the appearance of the second component of the solution (for $m = +1$), which is only perceptible in the near plate region, because at this stage it is over-damped and it vanishes very quickly.

The variation of the velocity profiles for $Re = 10$ in Fig. 10b and c with De and M_w and their relation with those of Fig. 10a for $Re = 1$ follows the above arguments and are not discussed further.

4.4.3. Solution duplicity and spatial chaotic behavior at super-critical elastic blowing Mach numbers

For $M_w > 1$ there are always two possible values of B corresponding to $m = \pm 1$ and consequently two values for $(-zB)_{real}$ and $(-zB)_{imag}$ each. Note also that Eq. (15-a) is not valid for $M_w = \pm 1$, in which case the solution for B is given by Eq. (15-b). Therefore, from

Eqs. (17) and (21), the velocity profile is given by

$$u = c_3 \, e^{(-zR)^+_{real}y} \cos\left[(-zB)^+_{imag}y + t\right]$$

$$+ (1 - c_3) \, e^{(-zR)^-_{real}y} \cos\left[(-zB)^-_{imag}y + t\right] \qquad (24)$$

where parameter c_3 can take any numerical value. As explained above we consider here $c_3 = 0.5$ to provide equal contributions from both solutions to u.

Since $(-zB)^+_{real} \neq (-zB)^-_{real}$, the two contributions to the solution dampen differently and with $(-zB)^+_{imag} \neq (-zB)^-_{imag}$ their shift factors are also different, i.e., they have different "spatial frequencies" of oscillation. Hence, we observe a spatial rather than a temporal kind of chaos whenever the two $(-zB)_{imag}$ are not rational multiples and this is called here spatial chaos.

In Fig. 10c some of the velocity profiles plotted do not exhibit a well-defined periodic shape, but show such spatial chaotic-like behavior. When $M_w > 1$, non-periodic stream-wise velocity profiles are found for certain combinations of Reynolds and Deborah numbers, as shown in the plots of Fig. 12 for $Re = 1$. All cases pertain to $De = 10$ and in the range $1 < M_w \leq 5$ the velocity profiles exhibit non-regular oscillations, whereas in the range $5 < M_w \leq 20$ only the profiles for the lower values of M_w ($5 < M_w \leq 10$) are irregular: the profiles for $M_w = 15$ and 20 do not exhibit the irregularities. So, this behavior occurs only at large Deborah numbers, but is limited to an intermediate range of supercritical injection elastic Mach numbers, which in Fig. 11 corresponds to the regions before the log–log straight lines where $M_w > 1$. In these regions both solutions are attenuated in a similar way whereas at smaller or larger values of M_w, one of the solution components dominates resulting in an almost periodic solution and in both cases the dominating solution is that for $m = -1$. The different growth factors of y_p^- and y_p^+ with M_w in Eqs. (22-a) and (22-b) confirm that the chaotic behavior will disappear when the two solutions become too different, with one predominating over the other, thus reducing their mutual interference. A similar behavior occurs at a higher Reynolds number of 10, but plots are not shown for conciseness.

5. Conclusions

An analytical solution is derived for the flow of UCM fluids over an oscillating porous plate in an infinite medium and both the suction and blowing cases are investigated separately. Generally speaking, at low Deborah numbers the cross flow controls the flow properties, whereas at high Deborah numbers the flow characteristics become independent of the magnitude of the cross flow in each flow regime. More specifically, there are important differences between the suction and blowing cases, as below.

When there is suction through the plate the existence of a solution is limited to cases where the suction velocity does not exceed the elastic wave speed, in contrast to the Newtonian flows for which there is always a solution. At low Deborah numbers the flows are similar to those for Newtonian fluids, where the waves are quickly dampened by viscous stresses. As the flow Deborah number increases the waves evolve from diffused waves towards more persistent solid-like waves with more cycles visible. The penetration depth increases and the wave peak-to-peak distance decreases. The suction solution corresponds to $m = -1$.

When there is blowing through the plate there are two sets of solutions. For weak blowing, i.e. when the injection velocities are smaller than the elastic wave speed, the solution is unique and periodic and corresponds to $m = -1$, with the effects of injection velocity opposite to those of the suction velocity. When the blowing velocity exceeds the elastic wave speed the uniqueness of the solution ceases and the velocity profile is now a linear combination of two solutions ($m = \pm 1$). Their attenuation rates as well as their shift angles are different and under low super-critical conditions one of the solutions dampens very quickly ($m = +1$) and the compounded solution remains periodic except very close to the plate. At large super-critical conditions, the attenuation rates are of similar magnitude and when the shift angles are not rational multiples there is spatial chaotic-like behavior. At even larger super-critical conditions the $m = -1$ solution again predominates and no spatial chaotic-like behavior is seen again in the compounded solution.

As far as inertia effects are concerned, the penetration depth and the peak-to-peak distance of the waves continue to scale with $1/\sqrt{Re}$ regardless of the cross flow type and magnitude, as for Newtonian fluids. This is a consequence of the linearity of the momentum equation and is easily shown from dimensional analysis. For very large injection Mach numbers the injection flow characteristics scale with the square root of the Deborah number, but in this respect the scaling laws are different for each of the two solutions. So, even though the analytical solution is somewhat complex, there are simple scaling laws for this complex viscoelastic flow.
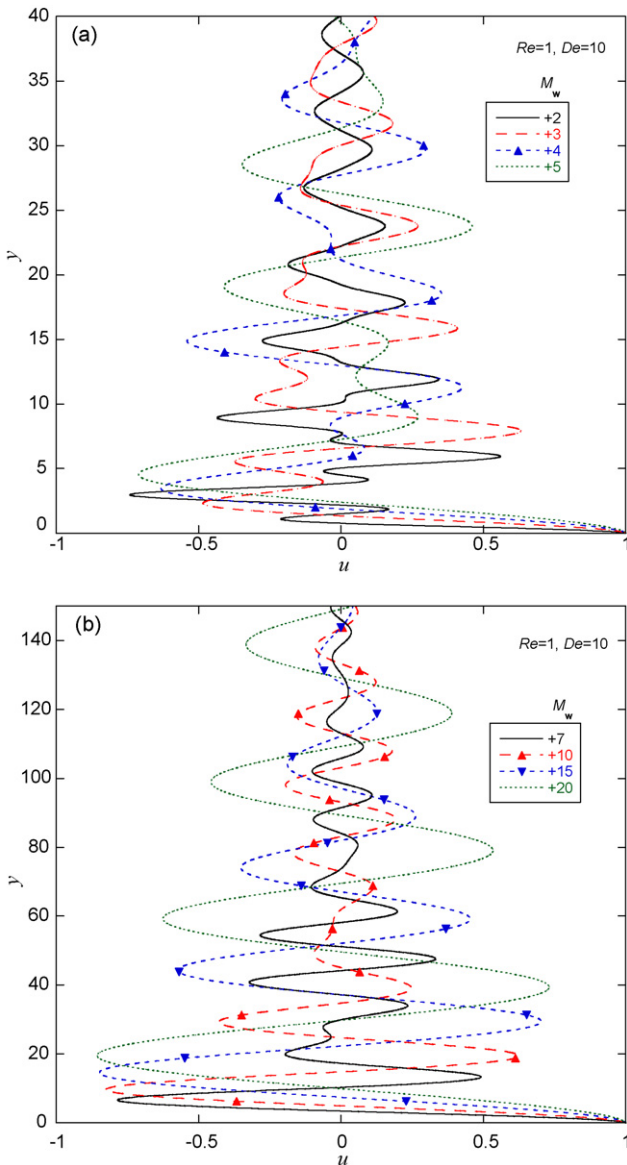

Fig. 12. Effect of injection velocity through the porous plate on the stability of the velocity profiles for super-critical injection elastic Mach numbers ($M_w \geq 1$) at $Re = 1$ and $De = 10$ ($M = 3.2$ and $E = 10$): (a) $1 < M_w \leq 5$; (b) $5 < M_w \leq 20$.

The increased penetration depth of the oscillations is consistent with findings in turbulent flow of viscoelastic fluids where the damping effect of walls in reducing turbulence is seen to have a longer range of action than for Newtonian fluids. Therefore, this analytical solution can inspire the development of Van Driest type of damping functions for turbulence models of drag reducing fluids.

Acknowledgements

Appendix A. Demonstration that $\tau_{yy} = 0$

Assuming that this solution depends on ϕ, with $\phi = At + By$, Eq. (3-b) leads to $\tau_{yy} = ce^{-\varphi\alpha/De}$, where c is a constant of integration. Inserting this result into Eq. (3-a) and using $\partial u/\partial y$ from Eq. (1) the differential equation for τ_{xy} becomes

$$\left(\frac{1}{z} - \frac{B^2 \alpha De}{Re} ce^{-\alpha\phi/De}\right) \frac{d\tau_{xy}}{d\phi} + \tau_{xy} = 0 \tag{I1}$$

the solution of which is given by Eq. (I4) with c' as another constant of integration.

$$\tau_{xy} = e^{c'} \left(e^{\alpha\phi/De} Re - B^2 De \, cz\alpha\right)^{-De\,z/\alpha} \tag{I2}$$

This solution immediately implies that the profile of streamwise velocity will be given by

$$u = \frac{B\alpha}{Re} e^{c'} \left(e^{\alpha\phi/De} Re - B^2 De \, cZ\alpha\right)^{-De\,Z/\alpha} \tag{I3}$$

The initial condition (4-a) requires that a time-independent term should not exist in Eq. (I3), and this implies that $c = 0$ and consequently $\tau_{yy} = 0$.

Appendix B. Expressions for the stress field

The shear stress is given by

$$\left(\tau_{xy}\right)_{\text{real}} = \frac{e^{(-zB)_{\text{real}}y}}{\alpha}$$
$$\times \left[Rev_w (a_{12} - a_{13}) - 2m\sqrt{Re}\varphi^{1/4} \cos\left(\frac{\theta}{2}\right) a_{14} - a_{15}\right] \tag{I4-a}$$

$$\left(\tau_{xy}\right)_{\text{imag}} = \frac{e^{(-zB)_{\text{real}}y}}{\alpha} \left[a_{16} + \sin\left(t + y(-zB)_{\text{imag}}\right)(-a_{17} + a_{18})\right] \tag{I4-b}$$

where functions a_{12} to a_{18} take the form

$$a_{12} = \left(4De + Re\,v_w^2 + \sqrt{\varphi}\right) \cos\left(t + y(-zB)_{\text{imag}}\right)$$

$$a_{13} = 2\left(De\,Re\,v_w^2 - 1\right) \sin\left(t + y(-zB)_{\text{imag}}\right)$$

$$a_{14} = \sin(-zB)_{\text{imag}} + Re\,v_w^2 \left(\cos\left(t + y(-zB)_{\text{imag}}\right) - De \sin\left(t + y(-zB)_{\text{imag}}\right)\right)$$

$$a_{15} = 2m\sqrt{Re}\left(1 + De\,Re\,v_w^2\right)\varphi^{1/4} \cos\left(t + y(-zB)_{\text{imag}}\right) \sin\left(\frac{\theta}{2}\right)$$

$$a_{16} = \sqrt{Re}\left(2\left(De\,Re\,v_w^2 - 1\right)\cos\left(t + y(-zB)_{\text{imag}}\right)\right.$$
$$\times \left.\left(m\varphi^{1/4}\cos\left(\frac{\theta}{2}\right) - \sqrt{Re}\,v_w\right)\right)$$

$$a_{17} = \sqrt{Re}\,v_w \left(4De + Re\,v_w^2 + \sqrt{\varphi}\right)$$

$$a_{18} = 2m\varphi^{1/4}\left(Re\,v_w^2 \cos\left(\frac{\theta}{2}\right) + \left(1 + Re\,De\,v_w^2\right)\sin\left(\frac{\theta}{2}\right)\right)$$

The normal stress τ_{xx} is described by

$$(\tau_{xx})_{\text{real}} = -e^{(-zB)_{\text{real}}y}\left[\sin\left(t + y(-zB)_{\text{imag}}\right)\Gamma_2 + \cos\left(t + y(-zB)_{\text{imag}}\right)\Gamma_1\right] \tag{I5-a}$$

$$(\tau_{xx})_{\text{imag}} = -e^{(-zB)_{\text{real}}y}\left[\cos\left(t + y(-zB)_{\text{imag}}\right)\Gamma_2 + \sin\left(t + y(-zB)_{\text{imag}}\right)\Gamma_1\right] \tag{I5-b}$$

where

$$\Gamma_1 = \frac{2De\,Re^2\left(a_{19} + a_{20} + a_{21} + a_{22}\right)}{a_{23} + a_{24} + a_{25}}$$

$$\Gamma_2 = \frac{4De\,Re^2\left(a_{26} + a_{27} + a_{28} + a_{29}\right)}{a_{30} + a_{31} + a_{32}}$$

with

$$a_{19} = \left[B_i^2 - B_r^2 - De\,Re + 2v_w\left(B_i^3 + 2B_i^2 B_r + B_i B_r^2 - 2B_r^3 - (B_i + B_r)De\,Re\right)\right]$$

$$a_{20} = v_w^2 \left[3B_i^4 + 8B_i^3 B_r + 6B_i^2 B_r^2 + 8B_i B_r\left(B_r^2 - De\,Re\right) - 5B_r^4\right]$$

$$a_{21} = 2v_w^3 \left[2B_i\|B\|^2 \left(B_i^2 + 2B_i B_r + 3B_r^2\right) + De\,Re\,(B_i + B_r) \times \left(\|B\|^2 - 4B_i B_r\right)\right]$$

$$a_{22} = v_w^4 \left[\|B\|^4 (B_i + B_r)(3B_i + 5B_r) + De\,Re\left(B_i^4 - 6B_i^2 B_r^2 + B_r^4\right)\right] + 2v_w^5\|B\|^6 (B_i + 2B_r) + v_w^6\|B\|^8$$

$$a_{23} = v_w^4 B_i^8 + 2v_w^2 B_i^6 \left[1 + 2v_w B_r\left(1 + v_w B_r\right)\right] + \left[De\,Re + B_r^2(1 + v_w B_r)^2\right]^2$$

$$a_{24} = 2B_i^2 \left[-De\,Re + B_r\left(1 + v_w B_r\right)\left(B_r + 3v_w B_r^3 - 6De\,Re\,v_w + 4v_w^2 B_r^3 + 2v_w^3 B_r^4\right)\right]$$

$$a_{25} = B_i^4 \left[1 + 2v_w\left(2B_r + 5v_w B_r^2 + De\,Re\,v_w + 6v_w^2 B_r^3 + 3v_w^3 B_r^4\right)\right]$$

$$a_{26} = B_i B_r + v_w \left[B_i B_r\left(B_i + 4B_r\right) + B_r^3 + De\,Re\,(B_r - B_i)\right]$$

$$a_{27} = 2B_i B_r \left[B_i^2 B_r + B_i B_r^2 + 2B_r^3 + De\,Re\,(B_r - B_i)\right]$$

$$a_{28} = v_w^2 + v_w^3 \left[2B_r \left\| B \right\|^2 \left(B_i^2 + 2B_i B_r + 3B_r^2 \right) + De\, Re\, (B_r - B_i) \right.$$
$$\left. \times \left(4B_i B_r + \left\| B \right\| \right) \right]$$

$$a_{29} = v_w^4 B_r \left[\left\| B \right\|^4 (B_i + 4B_r) - 2De\, Re\, B_i \left(B_i^2 - B_r^2 \right) \right] + v_w^5 B_r \left\| B \right\|^6$$

In the above expressions B_r is the real part of B (cf. Eq. (15)), B_i is the imaginary part and the norm of B is denoted $||B||$. They are given by

$$||B|| = \sqrt{B_i^2 + B_r^2}$$

References

[1] P.J. Oliveira, Method for time-dependent simulations of viscoelastic flows: vortex shedding behind cylinder, J. Non-Newtonian Fluid Mech. 101 (2001) 113–137.

[2] R.B. Bird, R.A. Armstrong, O. Hassager, Dynamics of Polymeric Liquids, Vol. I: Fluid Dynamics, John Wiley and Sons, 1987.

[3] T. Hayat, A.M. Siddiqui, S. Ashgar, Some simple flows of an Oldroyd-B fluid, Int. J. Eng. Sci. 39 (2001) 135–147.

[4] N. Aksel, C. Fetecau, M. Scholle, Starting solutions for some unsteady unidirectional flows of Oldroyd-B fluids, Z. Angew. Math. Phys. 57 (2006) 815–831.

[5] N.D. Waters, M.J. King, Unsteady flow of an elastico-viscous liquid, Rheol. Acta 9 (1970) 345–355.

[6] Y. Mochimaru, Unsteady-state development of plane Couette flow for viscoelastic fluids, J. Non-Newtonian Fluid Mech. 12 (1983) 135–152.

[7] R.I. Tanner, Note on the Rayleigh problem for a viscoelastic fluid, Z. Angew. Math. Phys. 13 (1962) 573–580.

[8] M.E. Erdogan, A note on an unsteady flow of a viscous fluid due to an oscillating plane wall., Int. J. Eng. Sci. 35 (2000) 1–6.

[9] D.D. Joseph, Fluid Dynamics of Viscoelastic Liquids, Springer Verlag, Berlin, 1990, Vol. 84 of Applied Mathematical Sciences Series.

[10] G.G. Stokes, On the effect of the internal friction of fluids on the motion of pendulums, Trans. Cambr. Phil. Soc. 9 (Part II) (1856) 8–106.

[11] Lord Rayleigh, On the motion of solid bodies through viscous liquids, Phil. Mag. 20 (1911) 697–711.